

Article

Integrated Yaw Stability Control of Electric Vehicle Equipped with Front/Rear Steer-by-Wire Systems and Four In-Wheel Motors

Younghoon Seo ^{1,†}, Kwanghyun Cho ^{2,†}  and Kanghyun Nam ^{1,*}¹ Department of Mechanical Engineering, Yeungnam University, Gyeongsan 38541, Korea; gjtnf5279@ynu.ac.kr² Mechatronics R&D Center, Samsung Electronics Co., Ltd., Yongin 16677, Korea; kh0960.cho@samsung.com

* Correspondence: khnam@yu.ac.kr; Tel.: +82-53-810-2455

† These authors contributed equally to this work.

Abstract: This paper presents the integrated motion control method for an electric vehicle (EV) equipped with a front/rear steer-by-wire (SbW) system and four in-wheel motor (IWM). The proposed integrated motion control method aims to maintain stable cornering. To maintain vehicle agility and stability, the lateral force and yaw rate commands of the vehicle are generated by referring to the neutral steering characteristics. The driver's driving force command, the lateral force command based on the bicycle model, and the yaw moment generated by the high-level controller are distributed into the driving force of each wheel and the lateral force of the front and rear wheels by the yaw moment distribution. Finally, the distributed forces are directly controlled by a low-level controller. To directly control the forces, a driving force observer and a lateral force observer were introduced via driving force estimation in the IWMs and rack force estimation in the SbW system. The control performance is verified through computer simulations.

Keywords: disturbance observer (DOB); four-wheel steering (4WS); in-wheel motor (IWM); kingpin torque; steer-by-wire (SbW); yaw moment observer (YMO)



Citation: Seo, Y.; Cho, K.; Nam, K. Integrated Yaw Stability Control of Electric Vehicle Equipped with Front/Rear Steer-by-Wire Systems and Four In-Wheel Motors. *Electronics* **2022**, *11*, 1277. <https://doi.org/10.3390/electronics11081277>

Academic Editor: Bai Li

Received: 5 March 2022

Accepted: 15 April 2022

Published: 18 April 2022

Publisher's Note: MDPI stays neutral with regard to jurisdictional claims in published maps and institutional affiliations.



Copyright: © 2022 by the authors. Licensee MDPI, Basel, Switzerland. This article is an open access article distributed under the terms and conditions of the Creative Commons Attribution (CC BY) license (<https://creativecommons.org/licenses/by/4.0/>).

1. Introduction

1.1. Literature Review

EV has attracted considerable attention owing to concerns regarding air pollution and resource depletion. EV's drivetrain has many advantages over an internal combustion engine. In addition, the SbW system has attracted interest in recent years. The SbW system has many advantages, as the steering wheel is disconnected from the rack-and-pinion system. These advantages can be summarized as follows [1]:

- Improved configuration of a vehicle's steering functionality;
- Improved design flexibility for a vehicle;
- Reduced vibration, which enhances the driver's comfort;
- Ability of the rack-and-pinion system to receive road surface information independently of the driver's operation.

Active motion control, which ensures the safety of passengers and vehicles, has been studied extensively in recent decades. Various vehicle motion control systems, such as four-wheel steering (4WS), active front steering (AFS), active rear steering (ARS), and direct yaw moment control (DYC), have been developed to maintain vehicle stability, even in emergencies. In addition, vehicle motion control systems for longitudinal motion, such as the anti-lock brake system (ABS) and traction control system (TCS), have also been studied.

In [2], two new methods were proposed on the basis of DOB and sliding mode control (SMC) for ABS control even in the case of uncertainties in the road conditions and the height of the center of gravity (CG). Thus, the wheel slip ratio could be maintained at the

desired value. The vehicle braking performance was improved on the basis of iterative learning control theory by integrating the vehicle model, slip ratio model, and vehicle speed observer [3]. A TCS for the IWM system was proposed as a driving torque control method for EV on the basis of a driving torque observer. Driving torque control improves vehicle stability by preventing excessive wheel slip on the basis of the relationship between the driving torque and the slip ratio [4]. SMC-based wheel slip control was designed without a tire-road friction observer; tire-road friction is the most difficult to predict or measure among the various model uncertainties. The controller was verified using a vehicle equipped with a front IWM [5].

The additional yaw moment required for yaw rate control can be generated via active steering as well as on the basis of the wheel braking force and driving force. The purpose of DYC is to create an additional yaw moment to implement the yaw motion intended by the driver. A method for applying adaptive sliding mode control was presented to compensate for the nonlinear characteristics, disturbances, and model uncertainties of tires, and an experiment was performed to confirm the control performance [6]. In [7], to improve the maneuverability and stability of yaw motion during cornering, a robust DYC design based on the vehicle side slip angle was adopted by employing DOB. As EVs employ IWMs, they are particularly suitable for active torque distribution control because all the wheels can generate the torque independently [8]. In [9], the yaw moment control was designed by considering the saturation of the tire and applying variable cornering stiffness. In [10], smooth SMC was introduced for yaw rate control of target vehicles with electronic four-wheel drive (e-4WD) coexisting with IWMs in the front and a mechanical drivetrain in the rear, and torque distribution based on daisy-chaining allocation was proposed.

AFS, which can improve the handling characteristics of a vehicle while driving, has attracted considerable attention in the automotive industry. AFS is capable of generating additional lateral forces on the front wheels by controlling the steering angle. Most AFS control systems are based on the feedback of the yaw rate, side slip angle, and lateral acceleration. When the lateral acceleration is relatively small, the lateral force has a linear relationship with the wheel side slip angle and the 4WS and AFS can be controlled relatively ideally. When the lateral acceleration is large, the tire force is saturated and the 4WS and AFS cannot control the vehicle. The effects of various types of torque distribution on vehicle performance were analyzed under various steering and straight driving conditions, and it was confirmed that the strategy of torque distribution based on the driving conditions increases vehicle stability [11]. In [12], feedback control based on the yaw rate and lateral acceleration through an SbW system was proposed, and the AFS of the SbW system was shown to be more effective than DYC. Active steering control of an SbW system was proposed to adjust the handling characteristics of the vehicle according to the driver's preference, and its effect was verified experimentally [13]. In [14], because the lateral tire force measurements were obtained using multi-sensing hub units developed by NSK Ltd., direct lateral tire force control could be realized.

In [15], an integrated control strategy based on 4WS and DYC was proposed. An adaptive sliding mode control that is robust against model uncertainty and external disturbances was designed to calculate the desired yaw moment and front wheel steering angle [16]. The Takagi–Sugeno fuzzy control technique was introduced to solve problems related to model uncertainty and nonlinearity, and the lateral stability of the vehicle was improved by integrating AFS and DYC [17]. In [18], four critical conditions were introduced, and an integrated motion control plan consisting of three layers was presented. The top-level controller calculates the yaw moment of the vehicle, the middle-level force allocation controller distributes the braking force or driving force and steering angle of each wheel, and the bottom-level slip ratio controller generates the driving force or braking force of each wheel.

There are many difficulties in realizing the integrated control method, and first, high performance of the vehicle control unit is required. In [19], an asymptotic optimality approach with low memory requirements and low computational complexity was demonstrated on the basis of the Lyapunov function and cascade theory. Second, a robust control

method against model uncertainty and external disturbances of the vehicle is required. In [20], a nonlinear disturbance observer based on second-order sliding mode control was proposed to overcome the chatter in SMC. In [21], backstepping control and second-order SMC were proposed to overcome the chatter in sliding mode control, nonlinear characteristics of the vehicle, model uncertainty, and external disturbances. As the vehicle motion is predominantly governed by the forces generated between the tires and the road, real-time knowledge of the tire forces is crucial when predicting vehicle motion; accordingly, several methods have been studied for real-time tire-road force estimation [22–26].

1.2. Contributions of the Article

This paper proposes advanced yaw rate control and lateral force estimation of EV equipped with 4WS of the SbW systems and 4WD of the IWM systems. Integrated motion control of EVs equipped with 4WS of the SbW system and 4WD of the IWM system can generate the independent driving force of four wheels and lateral force of front and rear wheels, and appropriate control input must be made for driver controllability and vehicle stability. The existing vehicle motion control method generates four independent driving forces and steering angles of the front and rear wheels. It is difficult to consider the vehicle's stability in this method. In addition to this, studies such as model predictive control methods are not only difficult to perform real-time control, but also difficult to implement vehicle integrated motion control algorithms such as vehicle side slip angle, roll angle, and pitch angle control. Therefore, the proposed integrated controller implements a 1 ms loop control algorithm by composing three layers of a high-level controller, a yaw moment distribution, and a low-level controller considering vehicle stability and handling characteristics. The contributions of the article are as follows.

- In contrast to the commonly used lateral force estimation that relies on the tire model, in this study, the lateral tire force is estimated using the DOB of the SbW system and the kinematics of the suspension.
- By minimizing the workload on each tire, the stability of the vehicle is improved.
- The 3-DOF motion control of the vehicle is possible through the tire vector control, which directly controls the longitudinal and lateral forces of the tire.

The remainder of this paper is organized as follows. Section 2 introduces the nonlinear 3-DOF model of 4WS and the three layers for vehicle motion control. Section 3 describes a high-level controller for yaw stability control based on a sliding mode controller. In addition, yaw moment distribution for distributing the lateral force of the front/rear SbW system and the driving force of each wheel is introduced. Section 4 describes the low-level controller, driving force controller, and lateral force controller. Section 5 presents the evaluation results of the proposed controller obtained by a computer simulation. Finally, Section 6 concludes the paper.

2. Vehicle Modeling

In this section, a 3-DOF vehicle model is introduced to describe the motion of 4WS and IWM driven EV. In addition, the three layers for vehicle motion control are presented.

2.1. 3-DOF Vehicle Model

The planar vehicle model shown in Figure 1 includes the longitudinal, lateral, and yaw motions, which are described as follows:

$$\begin{aligned} \sum F_x &= ma_x = -F_{yf} \sin \delta_f - F_{yr} \sin \delta_r + (F_{xfl} + F_{xfr}) \cos \delta_f + (F_{xrl} + F_{xrr}) \cos \delta_r \\ \sum F_y &= ma_y = F_{yf} \cos \delta_f + F_{yr} \cos \delta_r + (F_{xfl} + F_{xfr}) \sin \delta_f + (F_{xrl} + F_{xrr}) \sin \delta_r \\ \sum M_z &= I_z \dot{\gamma} = M_z + d \end{aligned} \quad (1)$$

where m is the total mass of the vehicle, I_z is the yaw moment of inertia at the CG, γ is the yaw rate, and a_x and a_y are the longitudinal and lateral accelerations of the vehicle, respectively. Further, M_z denotes the yaw moment generated by the driving force and

the lateral force, d denotes the model uncertainty and disturbance. F_x and F_y are the longitudinal and lateral forces. The first subscripts of F_x and F_y represent the front and rear axles (f, r), whereas the second subscripts represent the left and right (l, r). δ_f and δ_r are the front and rear steering angles at the wheel, i.e., $\delta_{fl} = \delta_{fr} = \delta_f$, $\delta_{rl} = \delta_{rr} = \delta_r$. l_f and l_r are the distances from the CG to the front and rear axles, and d_f and d_r are the track widths of the front and rear axles. The pitch, roll, and vertical motions are ignored in this model, and assuming that the difference between the left and right lateral forces is negligible, the yaw motion can be expressed as four driving forces and two lateral forces.

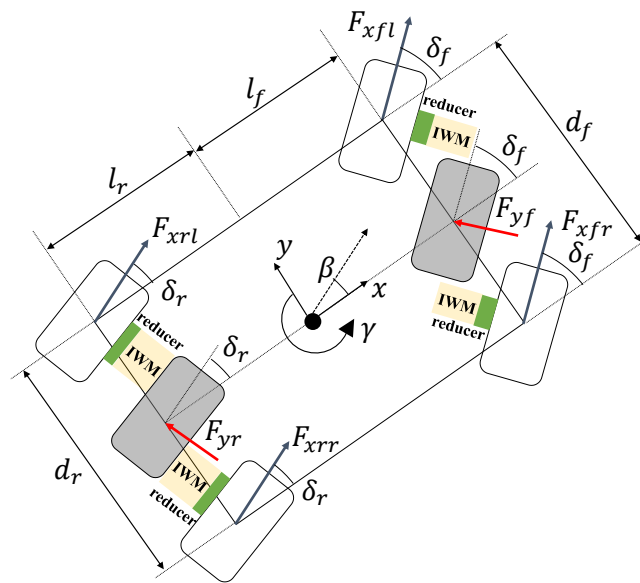


Figure 1. Planar vehicle model.

2.2. Three Layers Control System

In this study, the vehicle motion controller consists of three layers, and the overall algorithm of the vehicle motion controller is shown in Figure 2. The yaw rate command (γ_d) is from a reference model based on the driver’s steering angle (δ) and vehicle speed (v_x), i.e., the bicycle model for steady-state cornering. In addition, the lateral acceleration command (a_y^*) is designed as a reference model, and the lateral force command is generated by lateral dynamics, i.e., $F_y^* = ma_y^*$. The desired yaw rate and lateral acceleration for a given steering angle and vehicle speed are as follows:

$$\gamma_d = \frac{1}{\tau_r s + 1} \left(\frac{1}{1 - k_{us} v_x^2} \right) \frac{v_x}{l} \rho_{rp} \rho_{wr} \delta \tag{2}$$

$$a_y^* = \frac{1}{1 - k_{us} v_x^2} \frac{v_x^2}{l} \rho_{rp} \rho_{wr} \delta \tag{3}$$

where τ_r is the cutoff frequency of the desired model filter, l is the wheelbase, ρ_{rp} is the rack-and-pinion gear ratio, and ρ_{wr} is the rack-and-wheel gear ratio. k_{us} is the vehicle stability factor that describes the steering characteristics. The vehicle characteristics are classified into understeer, oversteer, and neutral-steer according to the sign of $l_f C_f - l_r C_r$ in k_{us} .

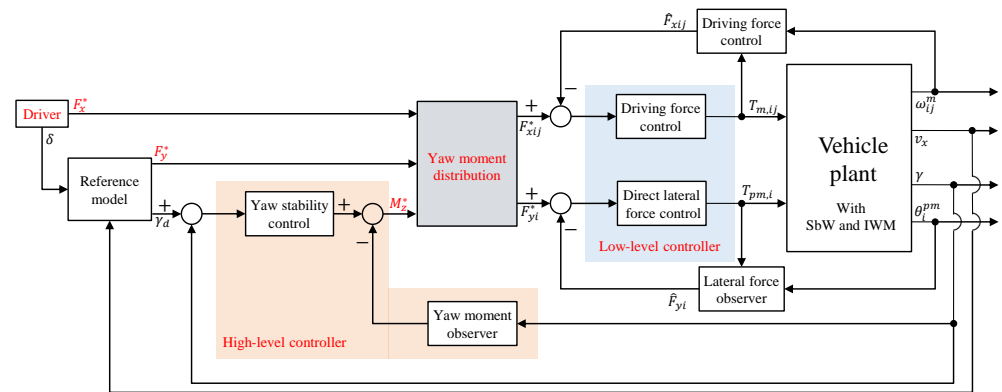


Figure 2. Overall block diagram of a vehicle motion controller.

3. High-Level Controller

The high-level controller, combined with a yaw stability controller and a yaw moment observer, is shown in Figure 3. The purpose of yaw stability control is to improve the handling performance of the vehicle and maintain its stability during cornering. The yaw stability controller is designed by employing the SMC method, which is known as a robust control method. To overcome chatter, a saturation function is employed instead of a sign function in the SMC method. Although the saturation function reduces the chatter, the tracking performance is degraded. A trade-off between chatter reduction and tracking performance can be achieved by employing a yaw moment observer (YMO) and adjusting the thickness of the saturation function.

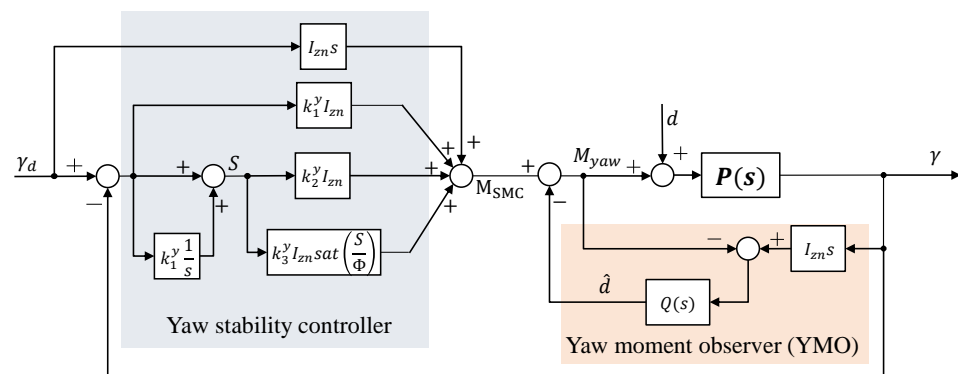


Figure 3. Block diagram of high-level controller.

3.1. Yaw Moment Observer

YMO is designed using the control input M_z of the yaw motion and the measured yaw rate, and the nominal yaw model is given by:

$$\frac{\gamma(s)}{M_z(s)} \approx \frac{1}{I_{zn}s} = P_n(s) \tag{4}$$

where I_{zn} is the yaw moment of the nominal inertia at the CG and $P_n(s)$ is the transfer function of the nominal model. As shown in Figure 3, it is important to set an appropriate Q-filter cutoff frequency because the performance of YMO depends on it. The Q-filter is designed as a low-pass filter satisfying the robust stability condition. In general, the Q-filter in YMO is designed as a first-order low-pass filter as follows:

$$Q(s) = \frac{\omega_Q}{s + \omega_Q} \tag{5}$$

where ω_Q is the cutoff frequency.

3.2. Design of Yaw Stability Controller

The yaw stability controller is designed in the SMC method and consists of two steps. First, the sliding surface is designed so that the system trajectory obtains the desired characteristics along the defined surface. Then, a discontinuous controller is designed so that the system trajectory reaches the sliding surface within a finite time. Sliding mode control has a fast response, excellent transient performance, and robustness against disturbances and model uncertainty. The sliding surface ($S(t)$) and reaching condition ($\dot{S}(t)$) are given by:

$$S(t) = e(t) + k_1^y \int e(t)dt, \quad \dot{S}(t) = -k_2^y S(t) - k_3^y \text{sat}\left(\frac{S(t)}{\phi}\right) \tag{6}$$

where k_1^y , k_2^y , and k_3^y are the controller gain and $e = \gamma_d - \gamma$. The saturation function is defined as $\text{sat}\left(\frac{S(t)}{\phi}\right)$. The control input of the proposed SMC is given by the following equation:

$$M_z = I_{zn} \dot{\gamma}_d - \hat{d} + I_{zn} k_1^y e + I_{zn} k_2^y S + I_{zn} k_3^y \text{sat}\left(\frac{S}{\phi}\right). \tag{7}$$

Using M_z , the closed-loop error dynamics can be expressed as follows:

$$\begin{aligned} \dot{S} &= \dot{e} + k_1^y e = \dot{\gamma}_d - \dot{\gamma} + k_1^y e \\ &= \dot{\gamma}_d - \frac{1}{I_z} \left[I_{zn} \dot{\gamma}_d - \hat{d} + I_{zn} k_1^y e + I_{zn} k_2^y S + I_{zn} k_3^y \text{sat}\left(\frac{S}{\phi}\right) \right] - \frac{1}{I_z} d + k_1^y e \\ &= \left(1 - \frac{I_{zn}}{I_z} \right) (\dot{\gamma}_d + k_1^y e) - \frac{1}{I_z} (d - \hat{d}) - \frac{I_{zn}}{I_z} k_2^y S - \frac{I_{zn}}{I_z} k_3^y \text{sat}\left(\frac{S}{\phi}\right). \end{aligned} \tag{8}$$

Theorem 1. Suppose that d of yaw motion is bounded, i.e., $|d| < |d^+|$, and k_1^y , k_2^y , and k_3^y are selected according to:

$$\begin{aligned} k_1^y > 0, k_2^y > 0, k_3^y > D, \phi > 0 \\ D = \sup \left| \left(\frac{I_z}{I_{zn}} - 1 \right) \dot{\gamma}_d - \frac{1}{I_{zn}} (d^+ - d) + \left(\frac{I_z}{I_{zn}} - 1 \right) k_1^y e \right|. \end{aligned} \tag{9}$$

If the above-mentioned conditions are satisfied, the system is uniformly stable.

Proof. The following positive Lyapunov function V is used to prove that the closed-loop control system is uniformly stable:

$$V = \frac{1}{2} S^2. \tag{10}$$

The time derivative of V is given by:

$$\begin{aligned} \dot{V} &= S \dot{S} = S (\dot{\gamma}_d - \dot{\gamma} + k_1^y e) \\ &= S \left[\left(1 - \frac{I_{zn}}{I_z} \right) (\dot{\gamma}_d + k_1^y e) - \frac{1}{I_z} (d - \hat{d}) - \frac{I_{zn}}{I_z} k_2^y S - \frac{I_{zn}}{I_z} k_3^y \text{sat}\left(\frac{S}{\phi}\right) \right] \\ &< S \left[\left(1 - \frac{I_{zn}}{I_z} \right) (\dot{\gamma}_d + k_1^y e) - \frac{1}{I_z} (d^+ - \hat{d}) - \frac{I_{zn}}{I_z} k_2^y S - \frac{I_{zn}}{I_z} k_3^y \text{sat}\left(\frac{S}{\phi}\right) \right] \\ &< S \left[\frac{I_{zn}}{I_z} D - \frac{I_{zn}}{I_z} k_2^y S - \frac{I_{zn}}{I_z} k_3^y \text{sat}\left(\frac{S}{\phi}\right) \right]. \end{aligned} \tag{11}$$

Because the discontinuous saturation function is used, it is divided into the range when $S \geq \phi$ and $S < \phi$. When $S \geq \phi$, \dot{V} is expressed as:

$$\dot{V} = S \left[\frac{I_{zn}}{I_z} D - \frac{I_{zn}}{I_z} k_2^y S - \frac{I_{zn}}{I_z} k_3^y \right]. \tag{12}$$

When $S < \phi$, \dot{V} is expressed as:

$$\dot{V} = S \left[\frac{I_{zn}}{I_z} D - \frac{I_{zn}}{I_z} k_2^y S - \frac{I_{zn}}{I_z} k_3^y \frac{S}{\phi} \right]. \tag{13}$$

Defining $k_3^y > D$, this system is stable at $\frac{\phi D}{\phi k_2^y + k_3^y} < S$. Thus, this system is uniformly stable. YMO improves the control performance of the system by reducing the magnitude of D . □

3.3. Yaw Moment Distribution

In this study, the yaw moment distribution is considered as the workload of the tire. The forces acting on the tire, i.e., the driving force and lateral force, must be within the friction circle to stably drive the vehicle [15]. For this reason, the yaw moment distribution designs a cost function that minimizes the workload of the tire, which is given by:

$$J = \sum_{i,j=1}^2 \eta_{ij}^2 = \sum_{i,j=1}^2 \frac{F_{xij}^2 + F_{yij}^2}{(\mu_{ij} F_{zij})^2} = \frac{1}{2} x^T Q x \tag{14}$$

where η is the tire workload and μ is the coefficient of friction between the tire and the road surface. The vector x is denoted by $x = [F_{xfl} \ F_{xf} \ F_{xrl} \ F_{xrr} \ F_{yfl} \ F_{yr}]^T$ and Q is a diagonal matrix, expressed as μ_{ij} and F_{zij} . The lateral force is estimated as the sum of the left and right wheels, and the lateral force of each wheel is assumed as follows:

$$F_{yfl} \approx F_{yfr} = \frac{1}{2} F_{yf}, F_{yrl} \approx F_{yrr} = \frac{1}{2} F_{yr}. \tag{15}$$

The vertical tire force F_{zij} for weight transfer owing to the longitudinal and lateral acceleration of the vehicle is given by:

$$\begin{aligned} F_{zfl} &= \frac{m}{d_f l g} \left[\frac{d_f}{2} (l_r g - h a_x) - h (l_r g - h a_x) a_y \right], F_{zfr} = \frac{m}{d_f l g} \left[\frac{d_f}{2} (l_r g - h a_x) + h (l_r g - h a_x) a_y \right] \\ F_{zrl} &= \frac{m}{d_r l g} \left[\frac{d_r}{2} (l_f g + h a_x) - h (l_f g + h a_x) a_y \right], F_{zrr} = \frac{m}{d_r l g} \left[\frac{d_r}{2} (l_f g + h a_x) + h (l_f g + h a_x) a_y \right] \end{aligned} \tag{16}$$

where g is the gravitational acceleration and h is the height of the CG. The weight transfer is the complexity of the suspension dynamics and disturbance; therefore, only the longitudinal and lateral accelerations are considered. The constraints are as follows:

$$\begin{aligned} F_x^* &= -F_{yf} \sin \delta_f - F_{yr} \sin \delta_r + (F_{xfl} + F_{xfr}) \cos \delta_f + (F_{xrl} + F_{xrr}) \cos \delta_r \\ F_y^* &= F_{yf} \cos \delta_f + F_{yr} \cos \delta_r + (F_{xfl} + F_{xfr}) \sin \delta_f + (F_{xrl} + F_{xrr}) \sin \delta_r \\ M_z^* &= l_f [(F_{yf} \cos \delta_f + F_{xfl} + F_{xfr}) \sin \delta_f] - l_r [F_{yr} \cos \delta_r + (F_{xrl} + F_{xrr}) \sin \delta_r] \\ &\quad + \frac{d_f}{2} (F_{xfr} - F_{xfl}) \cos \delta_f + \frac{d_r}{2} (F_{xrr} - F_{xrl}) \cos \delta_r \end{aligned} \tag{17}$$

$$\begin{bmatrix} F_x^* \\ F_y^* \\ M_z^* \end{bmatrix} = b = Ax$$

where the coefficient matrix is denoted by A and b is the command of the vehicle motion control. For the yaw moment distribution where the cost function J has the minimum value, the solution x^* is as follows. For further details, refer to Appendix A.

$$x^* = Q^{-1}A^T(AQ^{-1}A^T)^{-1}b = [F_{xfl}^* \quad F_{xfr}^* \quad F_{xrl}^* \quad F_{xrr}^* \quad F_{yf}^* \quad F_{yr}^*]. \quad (18)$$

The distributed driving force and lateral force on each wheel of the yaw moment distribution are controlled by the driving force controller and lateral force controller of the low-level controller.

4. Low-Level Controller

This section describes a driving force controller and a lateral force controller that provide feedback of the driving force and lateral force, as shown in Figures 4–6.

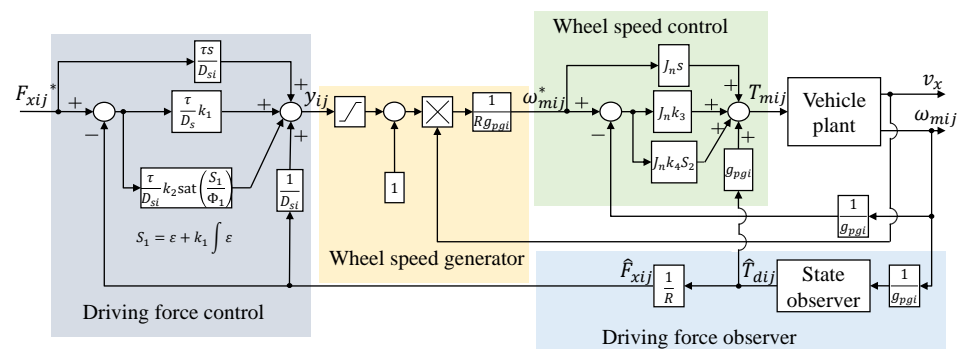


Figure 4. Block diagram of a driving force control system based on a driving force and wheel speed cascade controller.

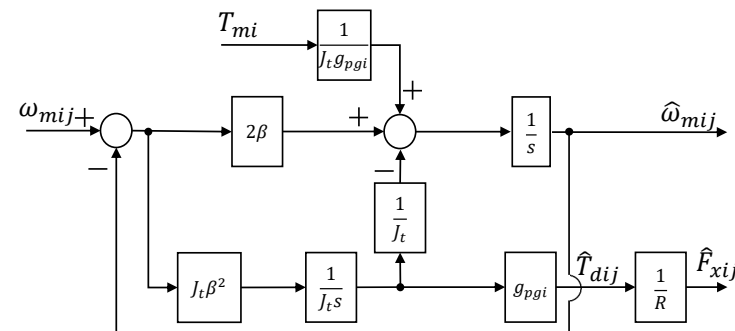


Figure 5. Structure of a state observer for estimating the driving forces.

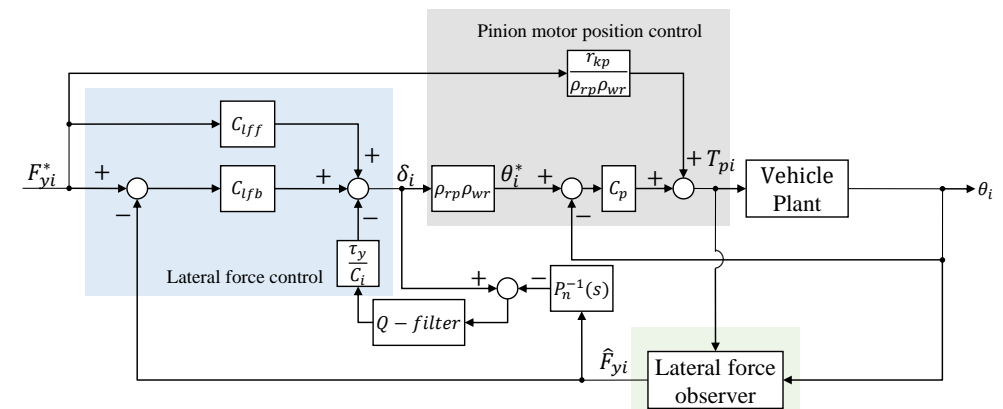


Figure 6. Block diagram of an observer-based lateral force controller.

4.1. Driving Force Observer

The driving force observer is designed to estimate the friction force between the tire and the road. Assuming that the current control of the IWM is sufficiently fast and accurate, the driving force can be estimated using the nominal model and angular velocity of the wheel. The wheel moment equation of the quarter-car model is given by:

$$J_t \dot{\omega}_{mij} = \frac{1}{g_{pgi}} T_{mij} - R F_{xij} \quad (19)$$

where J_t is the total inertia of the wheel, ω_w is the wheel angular velocity, g_{pg} is the gear ratio, T_m is the motor torque, F_x is the driving force, and R is the wheel radius. The subscript i is the front and rear wheels and j is the left and right wheels. The state observer is given by:

$$\frac{d}{dt} \hat{x} = A \hat{x} + B u + L(y - C \hat{x}) \quad (20)$$

$$\hat{x} = \begin{bmatrix} \hat{\omega}_{mij} \\ \hat{F}_{xij} \end{bmatrix}, A = \begin{bmatrix} 0 & -\frac{1}{R J_t g_{pgi}} \\ 0 & 0 \end{bmatrix}, B = \begin{bmatrix} \frac{1}{J_t g_{pgi}^2} \\ 0 \end{bmatrix}, L = \begin{bmatrix} l_1 \\ l_2 \end{bmatrix}, C = [1 \quad 0]$$

where ω_m is the angular velocity of the IWM.

4.2. Driving Force Controller

The driving force controller based on the estimated force feedback is shown in Figure 4. The driving force controller is designed with a multiple-SMC method. The driving force controller consists of a DFO and a wheel speed control. The slip ratio is generated by controlling the driving force. The relationship between the wheel speed and the slip ratio γ is given by:

$$\omega_{mij}^* = \frac{1}{R} v_x (1 + \gamma_{ij}) \quad (21)$$

where γ is the slip ratio when the vehicle decelerates, and the slip ratio and γ are approximately equal when the vehicle accelerates in the vicinity of slip ratio = 0. The first-order dynamics of the driving force is expressed as follows:

$$\dot{F}_{xij} = -\frac{1}{\tau} F_{xij} + \frac{1}{\tau} D_{sij} \gamma_{ij} \quad (22)$$

where τ is the relaxation time constant, and D_{sij} is the driving stiffness of each wheel. The sliding surface (S_1) and reaching condition (\dot{S}_1) of the outer loop is given by:

$$S_1 = e + k_1 \int e, \quad \dot{S}_1 = -k_2 \text{sat} \left(\frac{S_1}{\phi_1} \right) \quad (23)$$

where $e = F_{xij}^* - F_{xij}$. The control input γ_{ij} is given by:

$$\gamma_{ij} = \frac{\tau}{D_{si}} \dot{F}_{xij}^* + \frac{1}{D_{si}} \hat{F}_{xij} + \frac{\tau}{D_{si}} \left[k_1 e + k_2 \text{sat} \left(\frac{S_1}{\phi_1} \right) \right] \quad (24)$$

where D_s is the nominal driving stiffness. Using y_{ij} , the closed-loop error dynamics can be written as follows:

$$\begin{aligned} \dot{S}_1 &= \dot{e} + k_1 e = \dot{F}_{xij}^* - \dot{F}_{xij} + k_1 e \\ &= \dot{F}_{xij}^* + \frac{1}{\tau} F_{xij} - \frac{D_{sij}}{\tau} \left[\frac{\tau}{D_{si}} \dot{F}_{xij}^* + \frac{1}{D_{si}} \hat{F}_{xij} + \frac{\tau}{D_{si}} k_1 e + \frac{\tau}{D_{si}} k_2 \text{sat} \left(\frac{S_1}{\phi_1} \right) \right] + k_1 e \\ &= \left(1 - \frac{D_{sij}}{D_{si}} \right) \dot{F}_{xij}^* - \frac{1}{\tau} \left(F_{xij} - \frac{D_{sij}}{D_{si}} \hat{F}_{xij} \right) + \left(1 - \frac{D_{sij}}{D_{si}} \right) k_1 e - \frac{D_{sij}}{D_{si}} k_2 \text{sat} \left(\frac{S_1}{\phi_1} \right) \\ d_1 &= \left(1 - \frac{D_{sij}}{D_{si}} \right) \dot{F}_{xij}^* - \frac{1}{\tau} \left(F_{xij} - \frac{D_{sij}}{D_{si}} \hat{F}_{xij} \right) + \left(1 - \frac{D_{sij}}{D_{si}} \right) k_1 e. \end{aligned} \tag{25}$$

Theorem 2. Suppose that d_1 is bounded, i.e., $|d_1| < |d_1^+|$, and the gains k_1 and k_2 are selected according to:

$$k_1 > 0, \quad k_2 > D = \sup \left| \frac{D_{si}}{D_{sij}} d_1 \right|, \quad \phi_1 > 0. \tag{26}$$

If the above-mentioned conditions are satisfied, the system is uniformly stable.

Proof. The following positive Lyapunov function V_1 is used to prove that the closed-loop control system is uniformly stable:

$$V_1 = \frac{1}{2} S_1^2. \tag{27}$$

The time derivative of V_1 is given by:

$$\begin{aligned} \dot{V}_1 &= S_1 \dot{S}_1 = S_1 (\dot{F}_{xij}^* - \dot{F}_{xij} + k_1 e) = S_1 \left[d_1 - \frac{D_{sij}}{D_{si}} k_2 \text{sat} \left(\frac{S_1}{\phi_1} \right) \right] \\ &< S_1 \left[|d_1^+| - \frac{D_{sij}}{D_{si}} k_2 \text{sat} \left(\frac{S_1}{\phi_1} \right) \right] < S_1 \left[D_1 - \frac{D_{sij}}{D_{si}} k_2 \text{sat} \left(\frac{S_1}{\phi_1} \right) \right]. \end{aligned} \tag{28}$$

Defining $k_2 > D_1$, this system is stable at $\frac{\phi_1 D_1}{k_2} < S_1$. Thus, this system is uniformly stable. The dynamics of wheel speed control is expressed as follows:

$$\dot{\omega}_{mij} = \frac{1}{J_t g_{pgi}} T_{mij} - \frac{1}{J_t} T_{dij} \tag{29}$$

where T_d is the driving torque. The sliding surface (S_2) and reaching condition (\dot{S}_2) of the inner loop is given by:

$$S_2 = e + k_3 \int e, \quad \dot{S}_2 = -k_4 S_2 \tag{30}$$

where $e = \omega_{mij}^* - \omega_{mij}$. The control input T_{mij} is given by:

$$T_{mij} = g_{pgi} J_{mi} \dot{\omega}_{mij}^* + g_{pgi} \hat{T}_{dij} + g_{pgi} J_{mi} (k_3 e + k_4 S_2) \tag{31}$$

where J_n is the nominal inertia. Using T_{mij} the closed-loop error dynamics can be written as follows:

$$\begin{aligned} \dot{S}_2 &= \dot{e} + k_3e = \dot{\omega}_{mij}^* - \dot{\omega}_{mij} + k_3e \\ &= \dot{\omega}_{mij}^* - \frac{1}{g_{pgi}J_{ti}}T_{mij} + \frac{1}{J_{ti}}T_{dij} + k_3e \\ &= \dot{\omega}_{mij}^* - \frac{J_{ni}}{J_{ti}}\dot{\omega}_{mij} - \frac{1}{J_{ti}}\hat{T}_{mij} - \frac{J_{ni}}{J_{ti}}k_3e - \frac{J_{ni}}{J_{ti}}k_4S_2 + \frac{1}{J_{ti}}T_{dij} + k_3e \\ d_2 &= \left(1 - \frac{J_{ni}}{J_{ti}}\right)(\dot{\omega}_{mij}^* + k_3e) - \frac{1}{J_{ti}}(\hat{T}_{dij} - T_{dij}). \end{aligned} \tag{32}$$

□

Theorem 3. Suppose that d_2 is bounded, i.e., $|d_2| < |d_2^+|$, and the gains k_3 and k_4 are selected according to:

$$k_3 > 0, k_4 > \sup|d_2| = D_2. \tag{33}$$

If the above-mentioned conditions are satisfied, the system is uniformly stable.

Proof. The following positive Lyapunov function V_2 is used to prove that the closed-loop control system is uniformly stable:

$$V_2 = \frac{1}{2}S_2^2. \tag{34}$$

The time derivative of V_2 is given by:

$$\begin{aligned} \dot{V}_2 &= S_2\dot{S}_2 = S_2(\dot{\omega}_{mij}^* - \dot{\omega}_{mij} + k_3e) = S_2 \left[d_2 - \frac{J_{ni}}{J_{ti}}k_4S \right] \\ &< S_2 \left[|d_2^+| - \frac{J_{ni}}{J_{ti}}k_4S \right] < S_2 \left[D_2 - \frac{J_{ni}}{J_{ti}}k_4S \right]. \end{aligned} \tag{35}$$

This system is stable at $\frac{J_{ni}D_2}{J_{ni}k_4} < S_2$. Thus, this system is also uniformly stable. □

4.3. Lateral Force Observer

In this study, the rack and pinion are installed in the front and rear steering systems, and the motor is connected to the pinion gear. The lateral force, which is the sum of the left and right forces, can be estimated from the rack force acting on the pinion gear and the kinematics of the suspension. DOB is employed for estimating the rack force, and assuming that the variation of the ratio of the transport distance of the rack gear to the wheel angle is negligible, i.e., $\dot{\rho}_{wr} \approx 0$, the kingpin torque can be estimated using the rack force. The kingpin torque is generated by the driving force, vertical force, and lateral force, and the estimates of the vertical force and driving force are presented in Sections 3.3 and 4.1, respectively. The dynamics of the pinion gear is given by:

$$J_{ri}\ddot{\theta}_i + B_{ri}\dot{\theta}_i = T_{pi} - T_{dis,i} \tag{36}$$

where J_r and B_r are the steering system inertia and friction, respectively. Further, θ , T_p , and T_{dis} are the rotation angle, motor torque, and disturbance of the pinion gear. The subscripts i is the front and rear wheels. The kingpin torque observer is shown in Figure 7. The estimated kingpin torque is given by:

$$\hat{T}_{kp,i} = \rho_{wr}\rho_{rp}\hat{T}_{dis,i} \tag{37}$$

where \hat{T}_{dis} is the estimated disturbance. J_n and B_n are the nominal inertia and friction of the steering system, respectively. The Q-filter is designed as a second-order low-pass filter, which is given by:

$$Q(s) = \frac{\omega_q^2}{s^2 + 2\zeta\omega_q + \omega_q^2} \tag{38}$$

where ω_q and ζ are the cutoff frequency and damping ratio, respectively. The kingpin torque generated by the driving force, lateral force, and vertical force is analyzed by focusing on the geometric parameters. The steering geometry is defined in Figure 8. The kingpin axis vector of the front left steering geometry is obtained using the kingpin angle (Ψ) and caster angle (Φ) of the two-dimensional plane in Figure 8, and the kingpin axis vector (\vec{a}_k) is given by:

$$\vec{a}_k = \frac{x - L_x}{\frac{1}{\tan(\Phi+90)}} = \frac{x + L_y}{\frac{1}{\tan(\Psi+90)}} = \frac{z}{1} = k \tag{39}$$

where L_x and L_y are the kingpin offset and caster trail at the wheel center, respectively. The direction of the kingpin axis vector (\vec{u}) is given by:

$$\vec{u} = \left\langle \frac{1}{\tan(\Phi + 90)}, \frac{1}{\tan(\Psi + 90)}, 1 \right\rangle. \tag{40}$$

The vector (\vec{r}) perpendicular to the kingpin axis vector and passing through the force application point is given by:

$$\vec{r} = \frac{x - r_x}{l} = \frac{y - r_y}{m} = \frac{z - r_z}{n} = w \tag{41}$$

where (r_x, r_y, r_z) , is the point of application of the force at the tire and $\langle \vec{l}, \vec{m}, \vec{n} \rangle$ is the direction vector of \vec{r} . The intersection (p) of \vec{r} and \vec{a}_k is as follows. For further details, refer to Appendix B and Figure 8.

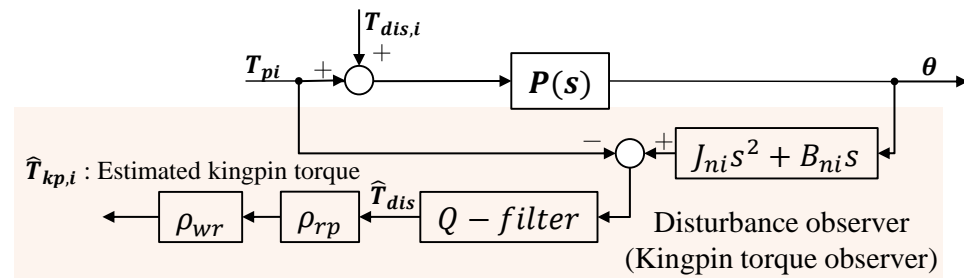


Figure 7. Block diagram of kingpin torque observer.

$$k = \frac{-\frac{L_x - r_x}{\tan(\Phi+90)} + \frac{L_x - r_y}{\tan(\Psi+90)} + r_z}{\frac{1}{\tan^2(\Phi+90)} + \frac{1}{\tan^2(\Psi+90)} + 1}, \quad p = \left(\frac{1}{\tan(\Phi + 90)}k + L_x, \frac{1}{\tan(\Psi + 90)}k - L_y, k \right). \tag{42}$$

The moment arm (R_k) between the force acting on the tire and the kingpin axis vector (\vec{a}_k) is given by:

$$R_k = (R_x, R_y, R_z) \\ R_x = -\frac{1}{\tan(\Phi + 90)}k - L_x + r_x, \quad R_y = -\frac{1}{\tan(\Psi + 90)}k + L_y + r_y, \quad R_z = -k + r_z \tag{43}$$

The kingpin torque can be calculated using the driving force, lateral force, and vertical force acting on the tire and the moment arm and is expressed as:

$$\lambda = \frac{1}{\sqrt{\frac{1}{\tan^2(\Phi+90)} + \frac{1}{\tan^2(\Psi+90)} + 1}}, \quad T_{kpij} = \lambda \begin{bmatrix} \frac{1}{\tan(\Phi+90)} & \frac{1}{\tan(\Psi+90)} & 1 \\ R_x & R_y & R_z \\ F_{xij} & F_{yij} & F_{zij} \end{bmatrix}. \quad (44)$$

The lateral force acting on the left and right tire is given by:

$$F_{yil} = \kappa_y[\lambda T_{kpil} - \kappa_z F_{zil} - \kappa_x F_{xil}], F_{yir} = \kappa_y[\lambda T_{kpir} + \kappa_z F_{zir} + \kappa_x F_{xir}]$$

$$\kappa_x = \frac{R_z}{\tan(\Psi + 90)} - R_y, \kappa_y = \frac{1}{R_x - \frac{R_z}{\tan(\Phi+90)}}, \kappa_z = \frac{R_y}{\tan(\Phi + 90)} - \frac{R_x}{\tan(\Psi + 90)}. \quad (45)$$

The sum of the lateral forces of the left and right wheels is given by:

$$F_{yi} = \kappa_y[\lambda T_{kpi} - \kappa_z \Delta F_{zi} - \kappa_x \Delta F_{xi}] \quad (46)$$

where ΔF_{zi} and ΔF_{xi} are the differences between the left and right vertical and driving forces, respectively.

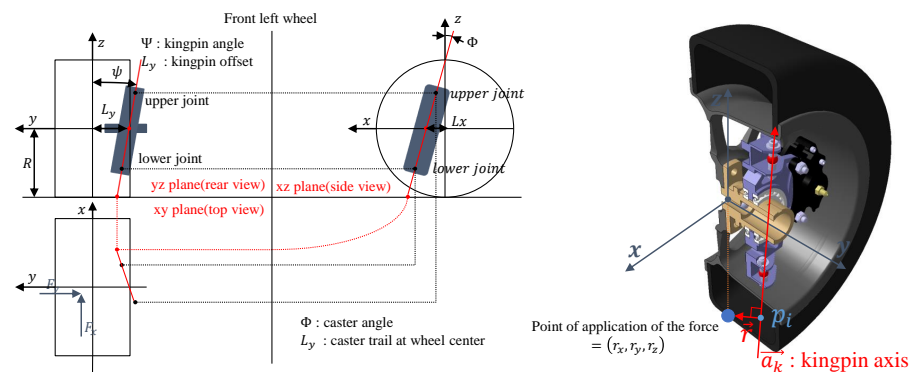


Figure 8. Description on the steering geometry.

4.4. Lateral Force Controller

The lateral force controller, which directly controls the lateral force, is shown in Figure 6. It consists of a lateral force observer and pinion motor position control that controls the pinion gear angle of the rack and pinion system. The lateral force control is designed on the basis of a linear tire model and first-order dynamics. The lateral force of the linear tire model uses the vehicle velocity, yaw rate, side slip angle (β), and steering angle. In this study, the position of the pinion gear is controlled and the angle of the pinion gear is regarded as the only control input to control the lateral force. The linear lateral tire model with for first-order dynamics is given by:

$$F_{yi} = -\frac{1}{1 + \tau_y s} C_i \alpha_i \quad (47)$$

where τ_y is the nominal relaxation time constant, C is the nominal cornering stiffness, and α is the side slip angle at the wheel. The dynamics of the lateral force are given by:

$$\dot{F}_{yi} = -\frac{1}{\tau_y} F_{yi} - \frac{C_i}{\tau_y} \beta - \frac{l_i C_i}{\tau_y v_x} \gamma + \frac{C_i}{\tau_y} \delta_i. \quad (48)$$

The subscript i is the front and rear wheels. The lateral force generated by the side slip angle and yaw rate is regarded as the disturbance because the side slip angle, which affects the lateral force, is not measurable owing to the sensor cost and the yaw rate is

strongly affected by the time-varying parameter. Thus, the dynamics of the lateral force can be rewritten as:

$$\dot{F}_{yi} = -\frac{1}{\tau_y} F_{yi} + \frac{C_i}{\tau_y} \delta_i + d_{yi} \quad (49)$$

where d_{yi} includes external disturbances and the effects of time-varying parameters, the side slip angle and yaw rate. The nominal model of the lateral force control is given by:

$$P(s) = \frac{F_{yi}}{\delta_i} = \frac{2C_i}{1 + \tau_y s} \quad (50)$$

The lateral force control system consists of a feedforward controller, feedback controller, and DOB. As stated previously, d_{yi} plays a crucial role in the lateral force control. DOB is employed to compensate for d_{yi} . The feedforward controller (C_{lff}) in the lateral force control system is designed as the inverse of the nominal model.

$$C_{lff} = P^{-1}(s) = \frac{1 + \tau_y s}{2C_i} \quad (51)$$

The feedback controller (C_{lfb}) is designed with a pole-zero cancellation method based on the nominal model, and it is expressed as:

$$C_{lfb} = \frac{k_P s + k_I}{s} \quad (52)$$

where k_P and k_I are the proportional and integral gains, respectively. The pinion motor position control consists of a feedforward controller and feedback controller. The feedforward controller is designed on the basis of a lateral force command, and the feedback controller is designed using a pole-zero cancellation method based on the nominal model of the steering system. The relationship between the feedforward controller and the lateral force is given by:

$$C_{ff} \approx \frac{r_{kp}}{\rho_{rp} \rho_{wr}} F_y^* \quad (53)$$

where r_{kp} is the ratio of the lateral force and the force acting on the pinion gear, which is set to 78 in this study. Because the torque of the pinion motor is governed by the lateral force generated during driving, the feedforward controller is designed as the kinematics between the lateral force command and the pinion motor, assuming that the difference between the actual lateral force and the estimated lateral force is negligible. The nominal model of the steering system is given by:

$$J_{rni} \ddot{\theta}_i + B_{rni} \dot{\theta}_i = T_{pi} \quad (54)$$

$$P_{pm}(s) = \frac{\theta_i}{T_{pi}} = \frac{1}{J_{rni} s^2 + B_{rni} s}$$

where J_{rn} and B_{rn} is the inertia and friction coefficient of the nominal model, respectively, and T_{pm} is the torque of the pinion motor. The feedback controller for pinion motor position control is given by:

$$C_p = k_{pD} s + k_{pP} \quad (55)$$

where k_{pP} and k_{pD} are the conventional proportional and differential gains of pinion motor position control, respectively.

5. Verification of Proposed Control Methods

5.1. Simulation Environment

The computer simulations were performed using the vehicle simulation software CarSim, MATLAB/Simulink, and Amesim. CarSim uses mathematical models to implement vehicle motion and provides the necessary data for integrated vehicle motion control. MATLAB/Simulink is used to implement an integrated vehicle motion controller, while Amesim designs the E-powertrain, reducer, and SbW system. The SbW system used in this study was modeled on the basis of the actual model of the dual-motor steering system in the author’s research group, and it is shown in Figure 9a. The performance of the rack force estimator was confirmed experimentally, as shown in Figure 9b, using a load cell sensor and a load motor.

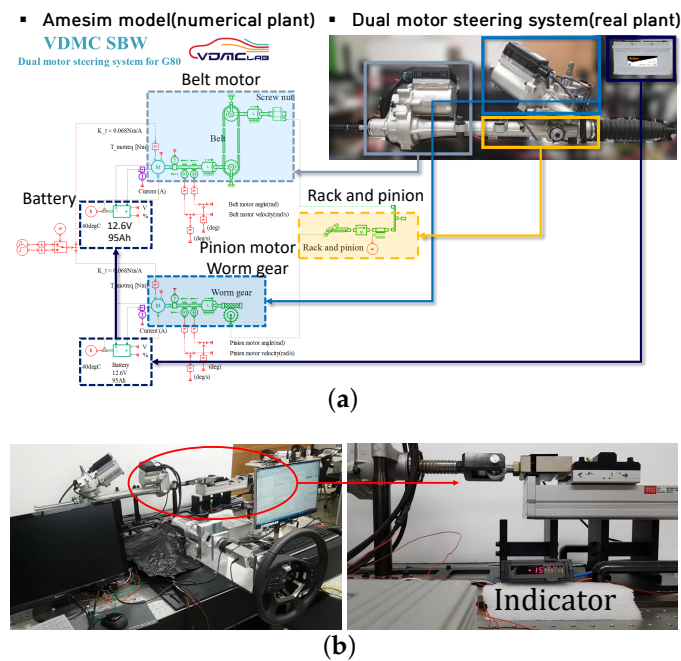


Figure 9. SbW system. (a) Amesim numerical model. (b) Experiment of rack force observer.

5.2. Simulation Results

The parameters of the vehicle and controller are listed in Table 1.

Table 1. Parameters of the vehicle model.

Parameter	Symbol	Value
Total vehicle mass	m	1530 kg
CG-front axle distance	l_f	1.35 m
CG-rear axle distance	l_r	1.43 m
Front track width	t_f	1.55 m
Rear track width	t_r	1.55 m
Yaw moment inertia	I_z	4192 kg·m ²
Rack gear-pinion gear ratio	ρ_{rp}	0.1
Wheel angle-rack gear ratio	ρ_{wr}	0.625
Front IWM gear ratio	ρ_{pgf}	0.25
Rear IWM gear ratio	ρ_{pgr}	1
Effective tire radius	R	0.303 m
Wheel inertia	J_t	0.9 kg·m ²

Table 1. *Cont.*

Parameter	Symbol	Value
Front driving stiffness	D_{sf}	88,000 N
Rear driving stiffness	D_{sr}	68,000 N
Front steering system inertia	J_{rf}	0.021 kg·m ²
Front steering system friction	B_{rf}	5.75 Nm·s/rad
Rear steering system inertia	J_{rr}	0.025 kg·m ²
Rear steering system friction	B_{rf}	5.73 Nm·s/rad
Front cornering stiffness	C_f	60,500 N/rad
Rear cornering stiffness	C_f	60,000 N/rad

The E-powertrain was a 4WD system consisting of an IWM system and a 4WS consisting of a front and rear SbW system. The simulation was performed in two ways: double lane change (DLC) and random steering and driving force commands (Random). The Random simulation use compared not only the proposed method and PID method for the higher-level controller but also the tire workload when four driving forces and two lateral forces were distributed using the yaw moment and the pseudo-inverse method. The percentage of the root mean square (RMS) errors of estimated forces are listed in Table 2. The percentage of RMS error is given by:

$$RMSerror = \sqrt{\frac{1}{n} \sum \frac{(F_{act} - \hat{F})^2}{F_{act}^2}} \quad (56)$$

where F_{act} and \hat{F} are the sensor values of CarSim and estimated force, respectively.

Table 2. Driving Force and Lateral Force Data.

Driving Force	DLC		Random	
	Left	Right	Left	Right
RMS error (front)	5.68%	7.44%	4.38%	5.48%
RMS error (rear)	6.05%	7.06%	4.46%	5.79%
Lateral Force	DLC		Random	
	F_{yf}	F_{yr}	F_{yf}	F_{yr}
RMS error	7.39%	10.53%	3.78%	7.81%

5.3. Results for Double Lane Change

The first simulation performed a DLC. The coefficient of friction between the road surface and the tire was 0.9 under dry asphalt road conditions. In this simulation, the steer signal was given at 7 s. The results are shown in Figures 10 and 11. The performance of the driving force observer and lateral force observer was satisfactory at a vehicle speed of 30 m/s. The trajectory of the vehicle is shown in Figure 10a, and the result of the lateral acceleration close to the maximum coefficient of friction between the road surface and the tire is shown in Figure 10b. Figure 10c shows that the high-level controller, yaw moment distribution, and low-level controller introduced in this study effectively track the yaw rate according to the driver's steering angle. The yaw moment generated by the high-level controller and the workload ratio calculated from the CarSim sensor are shown in Figure 10d,e, respectively. In Figure 10d, a larger yaw moment cannot be generated even though the vehicle yaw rate error increases because of the saturation function of the yaw stability controller. As shown in Figure 10e, the tire workload ratio confirms that the maximum friction force of each wheel is produced.

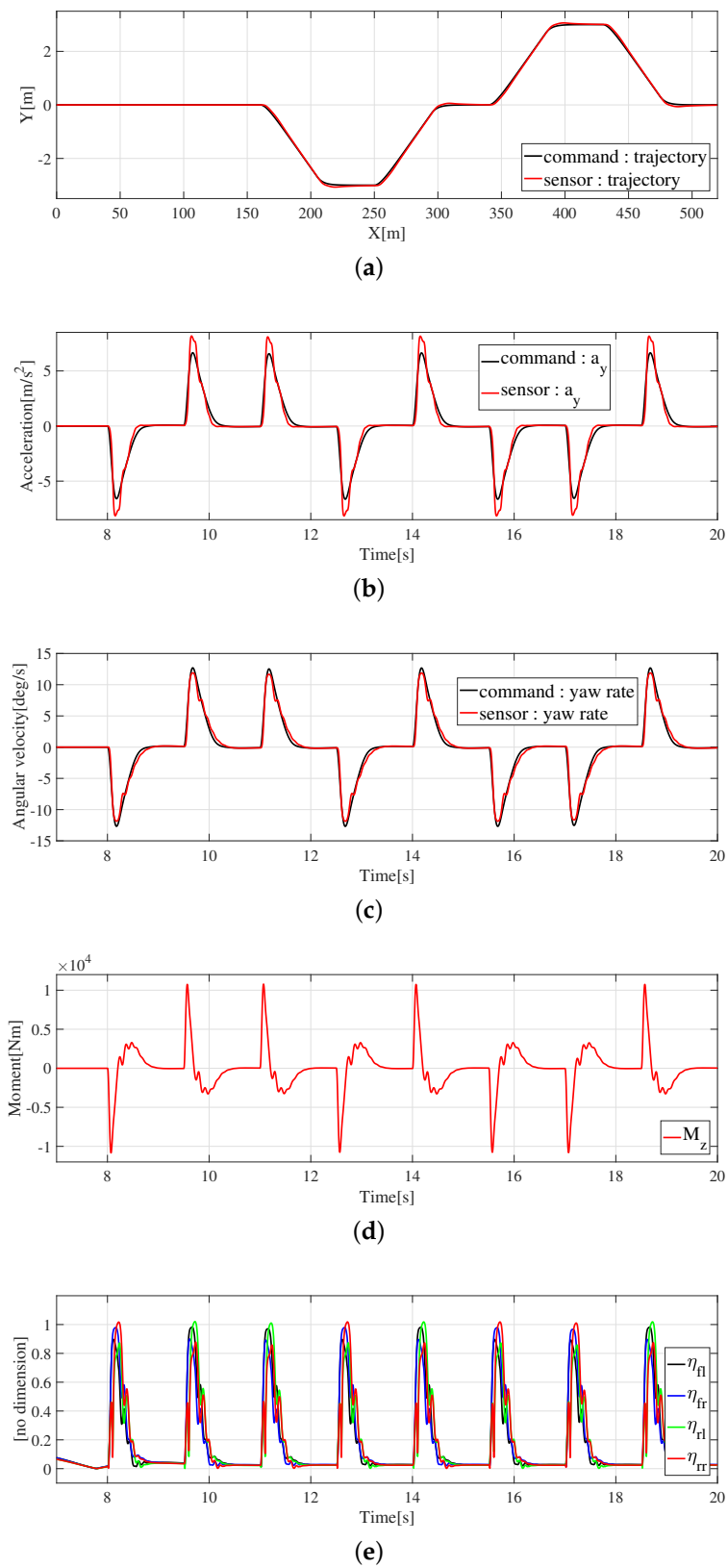


Figure 10. Results for DLC. (a) Vehicle trajectory. (b) Vehicle lateral acceleration. (c) Vehicle yaw rate. (d) Control yaw moment. (e) Tire workload.

The driving force and lateral force distributed in the yaw moment distribution are shown in Figures 12a–d and 11c,d; the performance of the low-level controller can also be

confirmed. In this simulation, the steering angle command and the actual steering angle at the wheel are shown in Figure 12e, and it can be confirmed that an additional steering angle is generated for the direct lateral force control. The rear wheel steering angle is shown in Figure 11a. The influence of the kingpin torque and vertical force on the lateral force estimation is shown in Figure 11b, and the influence of the driving force on the lateral force estimation in this simulation is negligible.

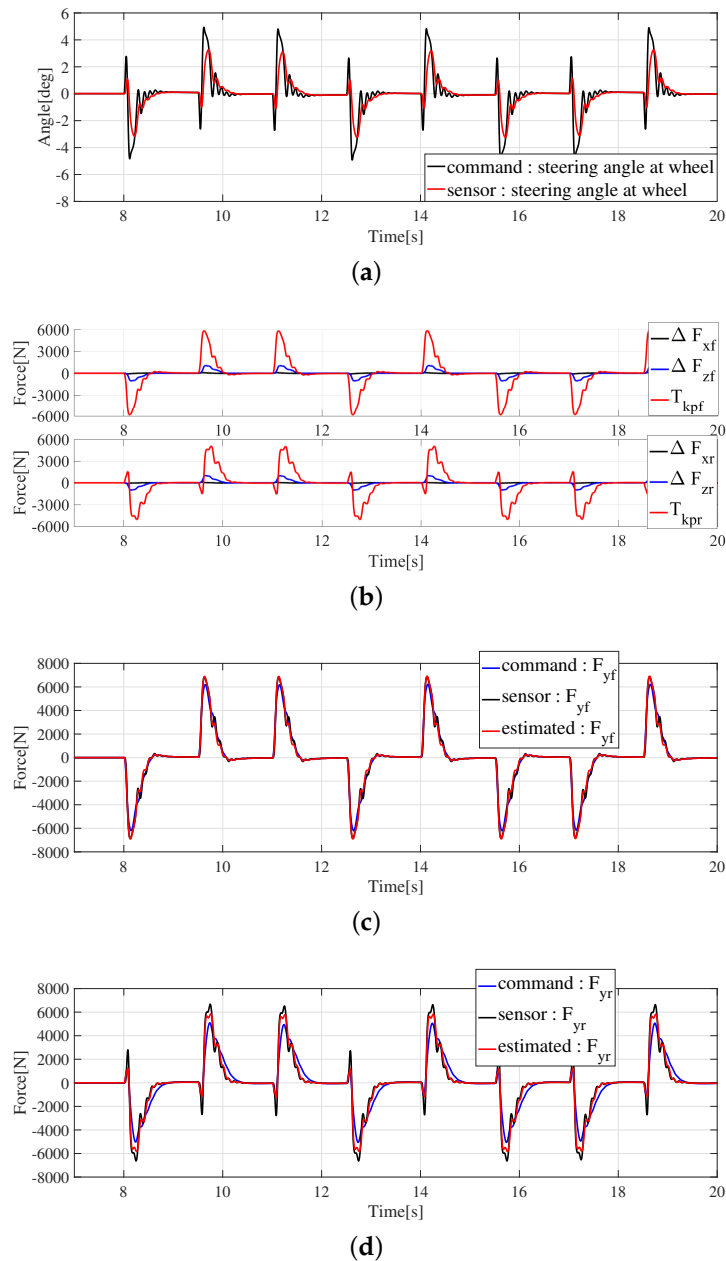


Figure 11. Results for DLC. (a) Rear steering angle at wheel. (b) The influence of kingpin torque, driving force and vertical force. (c) Front lateral force. (d) Rear lateral force.

5.4. Results for Random

The second simulation performed random steering and random driving force. It verified the performance of yaw stability control and lateral force estimation according to the load transfer and driving force when the vehicle is accelerating and decelerating. The steering signal was given at 4 s. The simulation results are shown in Figures 13–15. The vehicle was driven between 18.5 m/s and 23 m/s, as shown in Figure 13a. The accel-

eration of the vehicle is shown in Figure 13b; the vehicle motion control according to the acceleration and deceleration of the vehicle was successful. As mentioned above, the results of the proposed method and the PID method for the high-level controller are shown in Figure 13c, and the error of each method is shown in Figure 13d.

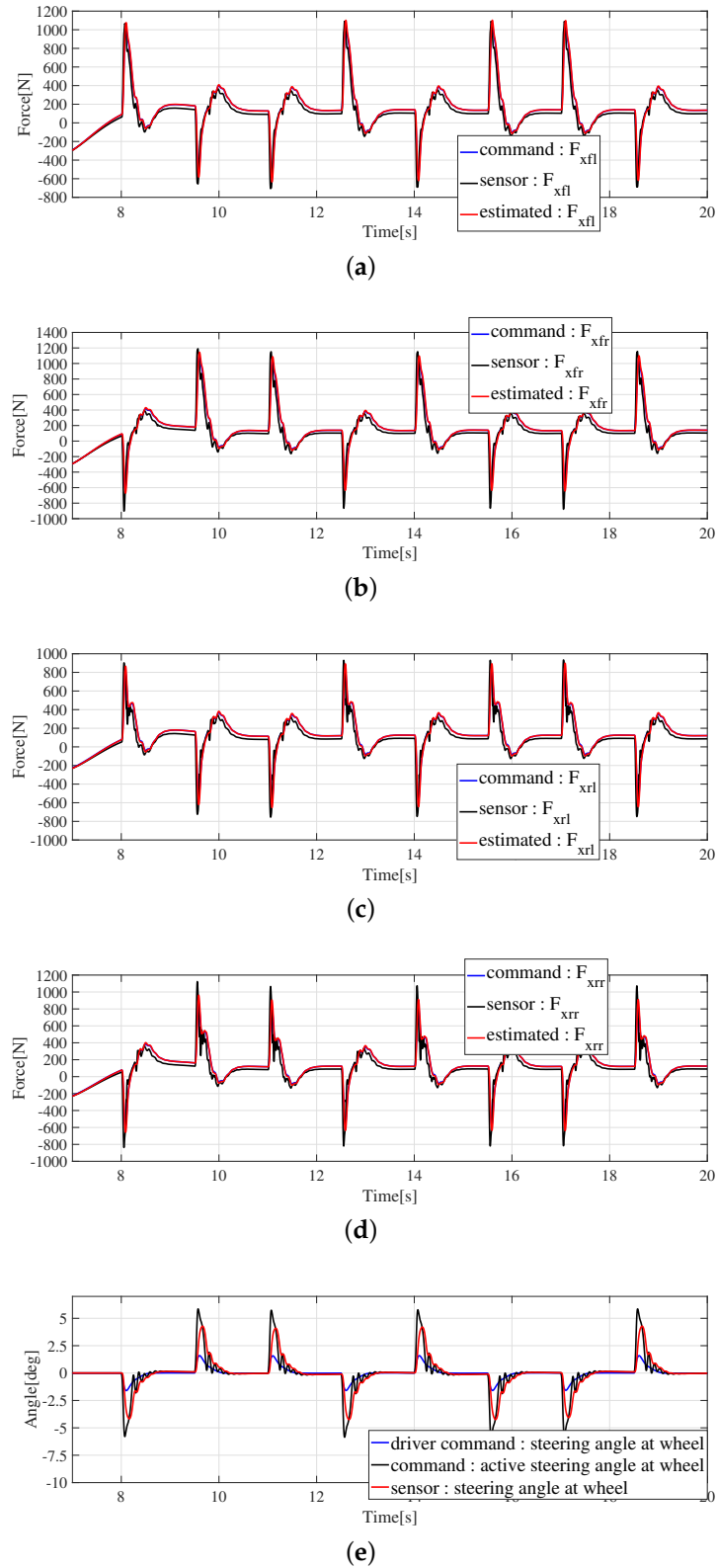


Figure 12. Results for DLC. (a) Front left driving force. (b) Front right driving force. (c) Rear left driving force. (d) Rear right driving force. (e) Front steering angle at wheel.

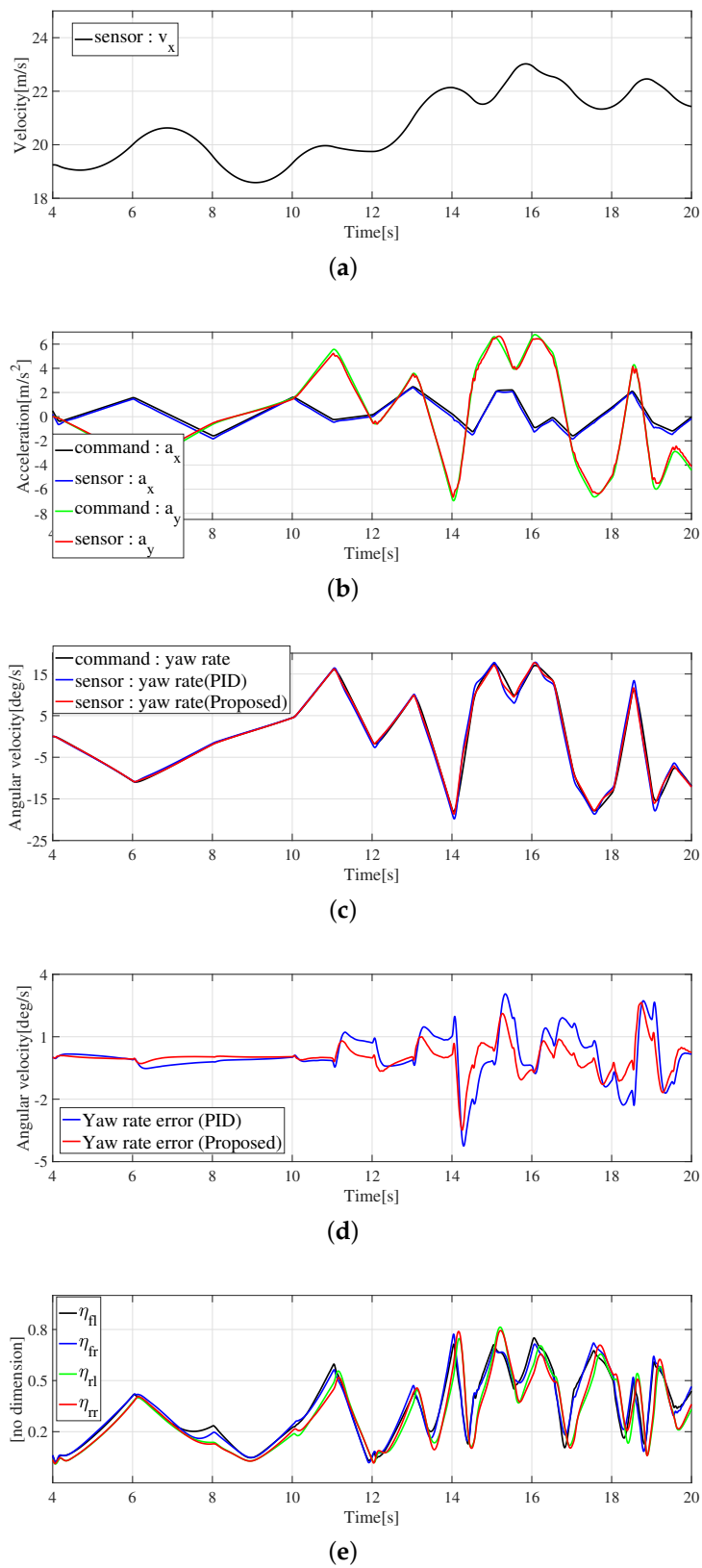


Figure 13. Results for random. (a) Vehicle velocity. (b) Vehicle longitudinal and lateral acceleration. (c) Vehicle yaw rate. (d) Yaw rate error. (e) Tire workload.

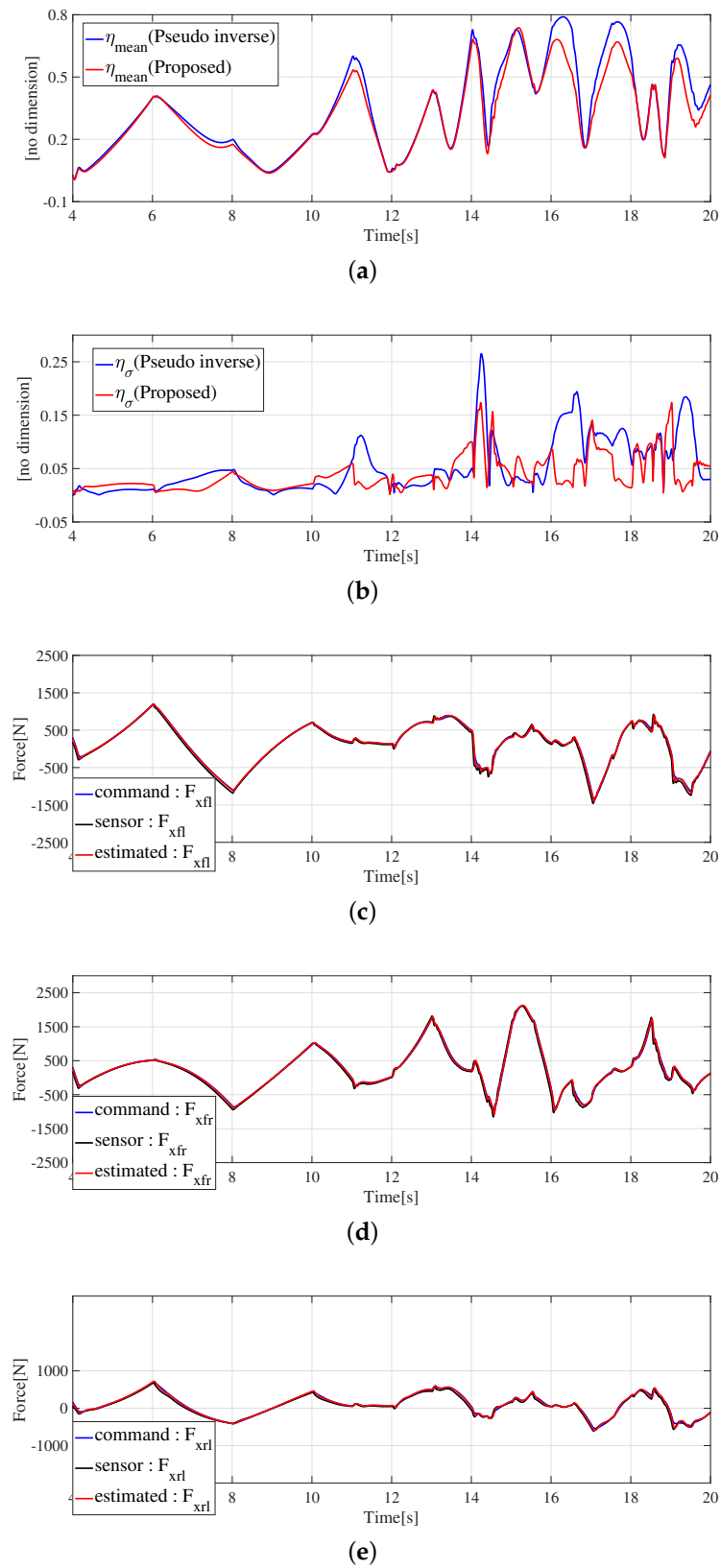
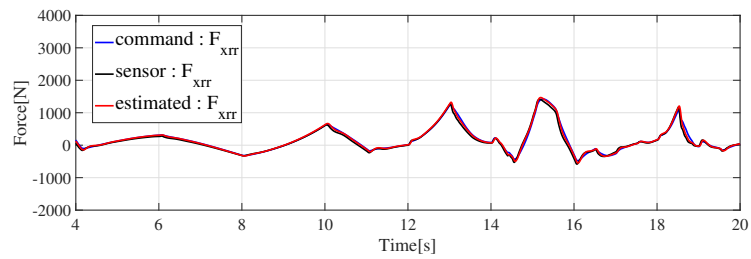
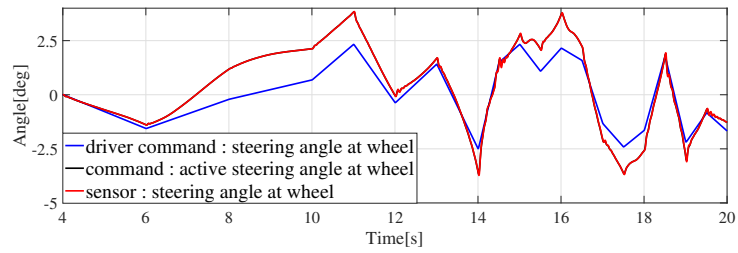


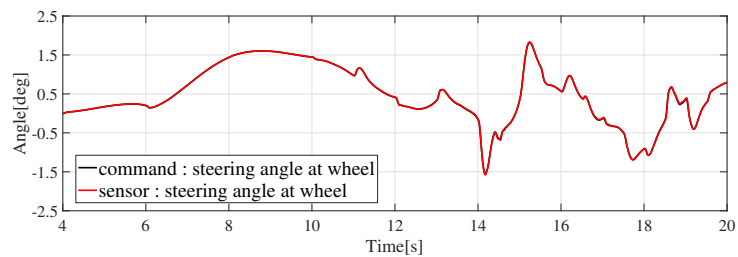
Figure 14. Results for random. (a) Tire workload mean. (b) Tire workload standard deviation. (c) Front left driving force. (d) Front right driving force. (e) Rear left driving force.



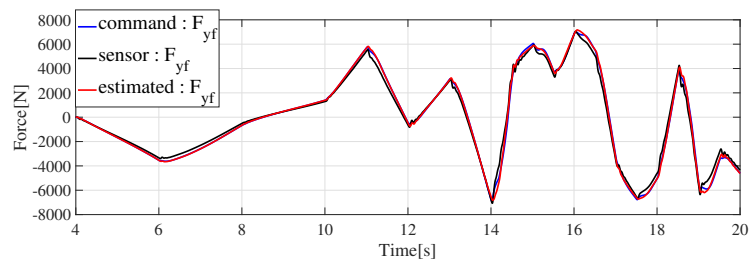
(a)



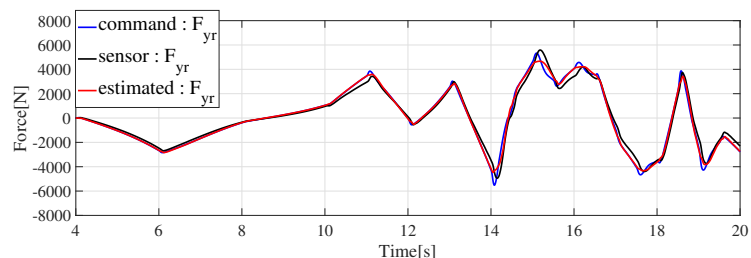
(b)



(c)



(d)



(e)

Figure 15. Results for random. (a) Rear right driving force. (b) Front steering angle at wheel. (c) Rear steering angle at wheel. (d) Front lateral force. (e) Rear lateral force.

To verify the vehicle’s stability, tire workloads were compared, and the proposed algorithm results are shown in Figure 13e. Figure 14a shows the tire workload means of the

distributed algorithm with four driving forces and two lateral forces using the proposed yaw moment distribution and pseudo-inverse method. It can be seen that the tire workload means of the proposed algorithm had a significantly smaller value than the pseudo-inverse at 11, 16.3, and 17.5 s. The standard deviation of the tire workload of each wheel is shown in Figure 14b; this shows that the proposed algorithm has similar values for the load on each wheel.

The performance of the low-level controller, according to the driver’s steering and driving force command, is shown in Figures 14c and 15a,d,e. It can be confirmed that the performance of the low-level controller was satisfactory. In Figure 15b, it can be seen that the steering angle is generated differently from the driver’s steering command because of the direct lateral force control. The steering angle according to the direct lateral force control of the rear wheel is shown in Figure 15c.

6. Conclusions

This paper proposed vehicle motion control based on three layers, namely a high-level controller, yaw moment distribution, and a low-level controller, to improve the handling of EV equipped with a front/rear SbW system and 4WD of the IWM system. The control method was to improve the stability of the vehicle by minimizing the tire workload for the 3-DOF motion of the vehicle, and this was realized by directly controlling the driving force and the lateral force. The high-level controller generates a yaw moment to control the yaw rate of the vehicle, and the yaw moment distribution was introduced to distribute the driving force of each wheel and the lateral force of the front and rear wheels. The low-level controller directly controlled the distributed driving force and lateral force by driving force control and lateral force control, respectively. In this paper, we designed a driving force observer and a lateral force observer that do not use a tire model to estimate the driving force and lateral force. The control performances were verified via computer simulation using CarSim, MATLAB/Simulink, and Amesim. The simulation was conducted with double lane change as well as random steering and driving force commands. In future works, the states of the vehicle are estimated using the estimated driving force and lateral force.

Author Contributions: Y.S. and K.C. have equally contributed to this paper, performed the numerical simulations, and proposed control algorithms. K.N. contributed considerable effort in conducting the HILs test and organizing the manuscript as a corresponding author. All authors have read and agreed to the published version of the manuscript.

Funding: This paper was supported by the Korea Institute for Advancement of Technology (KIAT) grant funded by the Korea Government (MOTID)(P0008473, HRD Program for Industrial Innovation) and in part by the Yeungnam University Research Grant 220A380108.

Conflicts of Interest: The authors declare no conflict of interest.

Appendix A

$$x = \begin{bmatrix} F_{xfl}^* & F_{xfr}^* & F_{xrl}^* & F_{xrr}^* & F_{yf}^* & F_{yr}^* \end{bmatrix}$$

$$A = \begin{bmatrix} \cos \delta_f & \cos \delta_f & \cos \delta_r & \cos \delta_r & -\sin \delta_f & -\sin \delta_r \\ \sin \delta_f & \sin \delta_f & \sin \delta_r & \sin \delta_r & \cos \delta_f & \cos \delta_r \\ a_{31} & a_{32} & a_{33} & a_{34} & a_{35} & a_{36} \end{bmatrix}$$

$$a_{31} = l_f \sin \delta_f - \frac{t_f}{2} \cos \delta_f, a_{32} = l_f \sin \delta_f + \frac{t_f}{2} \cos \delta_f$$

$$a_{33} = -l_r \sin \delta_r - \frac{t_r}{2} \cos \delta_r, a_{34} = -l_r \sin \delta_r + \frac{t_r}{2} \cos \delta_r$$

$$a_{35} = l_f \cos \delta_f, a_{36} = l_r \cos \delta_r$$

$$diag(Q) = [q_{11}, q_{22}, q_{33}, q_{44}, q_{55}, q_{66}]$$

$$\begin{aligned}
 q_{11} &= \frac{2}{(\mu_{fl}F_{zfl})^2}, q_{22} = \frac{2}{(\mu_{fr}F_{zfr})^2} \\
 q_{33} &= \frac{2}{(\mu_{rl}F_{zrl})^2}, q_{44} = \frac{2}{(\mu_{rr}F_{zrr})^2} \\
 q_{55} &= \left(\frac{1}{2(\mu_{fl}F_{zfl})^2} + \frac{1}{2(\mu_{fr}F_{zfr})^2} \right) \\
 q_{66} &= \left(\frac{1}{2(\mu_{rl}F_{zrl})^2} + \frac{1}{2(\mu_{rr}F_{zrr})^2} \right)
 \end{aligned}$$

Appendix B

The vector \vec{r} perpendicular to the kingpin axis and passing through the point of force acting on the tire is equal to the direction of the moment arm of the kingpin torque. The intersection point (p) of vector (\vec{r}) and vector (\vec{a}_k) is the support point of the moment arm, shown in Figure 8. The x , y , and z of p are as follows:

$$\begin{aligned}
 x &= lw + r_x = \frac{1}{\tan(\Phi + 90)}k + L_x \\
 y &= mw + r_y = \frac{1}{\tan(\Psi + 90)}k - L_y \\
 z &= nw + r_z = k
 \end{aligned}$$

The direction vector (\vec{v}) of \vec{r} is as follows:

$$\begin{aligned}
 l &= \frac{1}{w} \left(\frac{1}{\tan(\Phi + 90)}k + L_x - r_x \right) \\
 m &= \frac{1}{w} \left(\frac{1}{\tan(\Psi + 90)}k - L_x - r_y \right) \\
 n &= \frac{1}{w} (k - r_z)
 \end{aligned}$$

The vectors \vec{a}_k and the vectors \vec{r} are perpendicular, and the vectors \vec{u} and the vectors \vec{v} must be orthogonal.

$$\begin{aligned}
 \vec{u} \cdot \vec{v} &= \left\langle \frac{1}{\tan(\Phi + 90)}, \frac{1}{\tan(\Psi + 90)}, 1 \right\rangle \cdot \langle l, m, n \rangle = 0 \\
 &= \frac{1}{w} \left[\frac{1}{\tan(\Phi + 90)} \left(\frac{1}{\tan(\Phi + 90)}k + L_x - r_x \right) \right. \\
 &\quad \left. + \frac{1}{\tan(\Psi + 90)} \left(\frac{1}{\tan(\Psi + 90)}k - L_y - r_y \right) + k - r_z \right]
 \end{aligned}$$

k and p are as follows:

$$\begin{aligned}
 &\left(\frac{1}{\tan^2(\Phi + 90)} + \frac{1}{\tan^2(\Psi + 90)} + 1 \right) k = \\
 &\quad - \frac{L_x - r_x}{\tan(\Phi + 90)} + \frac{L_y + r_y}{\tan(\Psi + 90)} + r_z \\
 k &= \frac{- \frac{L_x - r_x}{\tan(\Phi + 90)} + \frac{L_y + r_y}{\tan(\Psi + 90)} + r_z}{\frac{1}{\tan^2(\Phi + 90)} + \frac{1}{\tan^2(\Psi + 90)} + 1} \\
 p &= \left(\frac{1}{\tan(\Phi + 90)}k + L_x, \frac{1}{\tan(\Psi + 90)}k - L_y, k \right)
 \end{aligned}$$

References

1. Onoda, Y.; Onuma, Y.; Goto, T.; Sugitani, T. *Design Concept and Advantages of Steer-by-Wire System*; SAE Technical Paper 2008-01-0493; SAE: Warrendale, PA, USA, 2008.
2. Phadke, S.B.; Shendge, P.D.; Wanaskar, V.S. Control of Antilock Braking Systems Using Disturbance Observer With a Novel Nonlinear Sliding Surface. *IEEE Trans. Ind. Electron.* **2020**, *67*, 6815–6823. [[CrossRef](#)]
3. Mi, C.; Lin, H.; Zhang, Y. Iterative learning control of antilock braking of electric and hybrid vehicles. *IEEE Trans. Veh. Technol.* **2005**, *54*, 486–494. [[CrossRef](#)]
4. Yoshimura, M.; Fujimoto, H. Driving Torque Control Method for Electric Vehicle with In-Wheel Motors. *Electr. Eng. Jpn.* **2012**, *181*, 721–728. [[CrossRef](#)]
5. De Castro, R.; Arajo, R.E.; Freitas, D. Wheel Slip Control of EVs Based on Sliding Mode Technique With Conditional Integrators. *IEEE Trans. Ind. Electron.* **2013**, *60*, 3256–3271. [[CrossRef](#)]
6. Nam, K.; Oh, S.; Fujimoto, H.; Hori, Y. Design of Adaptive Sliding Mode Controller for Robust Yaw Stabilization of In-wheel-motor-driven Electric Vehicles. *World Electr. Veh. J.* **2012**, *5*, 588–597. [[CrossRef](#)]
7. Kim, H.S.; Hyun, Y.J.; Nam, K.H. Disturbance Observer-Based Sideslip Angle Control for Improving Cornering Characteristics of In-Wheel Motor Electric Vehicles. *Int. J. Automot. Technol.* **2018**, *19*, 10711080. [[CrossRef](#)]
8. Maeda, K.; Fujimoto, H.; Hori, Y. Four-wheel driving-force distribution method for instantaneous or split slippery roads for electric vehicle with in-wheel motors. In Proceedings of the 2012 12th IEEE International Workshop on Advanced Motion Control (AMC), Sarajevo, Bosnia and Herzegovina, 25–27 March 2012; pp. 1–6.
9. Du, H.; Zhang, N.; Dong, G. Stabilizing Vehicle Lateral Dynamics with Considerations of Parameter Uncertainties and Control Saturation through Robust Yaw Control. *IEEE Trans. Veh. Technol.* **2010**, *59*, 2593–2597.
10. Park, G.; Han, K.; Nam, K.; Kim, H.; Choi, S.B. Torque Vectoring Algorithm of Electronic-Four-Wheel Drive Vehicles for Enhancement of Cornering Performance. *IEEE Trans. Veh. Technol.* **2020**, *69*, 3668–3679. [[CrossRef](#)]
11. Hu, J.; Tao, J.; Xiao, F.; Niu, X.; Fu, C. An Optimal Torque Distribution Control Strategy for Four-Wheel Independent Drive Electric Vehicles Considering Energy Economy. *IEEE Access* **2019**, *7*, 141826–141837. [[CrossRef](#)]
12. Segawa, M.; Nishizaki, K.; Nakano, S. A study of vehicle stability control by steer by wire system. *Proc. Int. Symp. Adv. Vehicle Contr.* **2000**, *712*, 1–7.
13. Yih, P.; Gerdes, J.C. Modification of vehicle handling characteristics via steer-by-wire. *IEEE Trans. Control Syst. Technol.* **2005**, *13*, 965–976. [[CrossRef](#)]
14. Nam, K.; Fujimoto, H.; Hori, Y. Advanced Motion Control of Electric Vehicles Based on Robust Lateral Tire Force Control via Active Front Steering. *IEEE/ASME Trans. Mechatron.* **2014**, *19*, 289–299. [[CrossRef](#)]
15. Fujimoto, H.; Maeda, K. Optimal yaw-rate control for electric vehicles with active front-rear steering and four-wheel driving-braking force distribution. In Proceedings of the IECON 2013–39th Annual Conference of the IEEE Industrial Electronics Society, Vienna, Austria, 10–13 November 2013; pp. 6514–6519.
16. Wang, J.; Wang, R.; Jing, H.; Chen, N. Coordinated Active Steering and Four-Wheel Independently Driving/Braking Control with Control Allocation. *Asian J. Control* **2016**, *18*, 111. [[CrossRef](#)]
17. Jin, X.; Yu, Z.; Yin, G.; Wang, J. Improving Vehicle Handling Stability Based on Combined AFS and DYC System via Robust Takagi-Sugeno Fuzzy Control. *IEEE Trans. Intell. Transp. Syst.* **2018**, *19*, 2696–2707. [[CrossRef](#)]
18. Zhang, J.; Sun, W.; Du, H. Integrated Motion Control Scheme for Four-Wheel-Independent Vehicles Considering Critical Conditions. *IEEE Trans. Veh. Technol.* **2019**, *68*, 7488–7497. [[CrossRef](#)]
19. Tjonnas, J.; Johansen, T.A. Stabilization of Automotive Vehicles Using Active Steering and Adaptive Brake Control Allocation. *IEEE Trans. Control Syst. Technol.* **2010**, *18*, 545–558. [[CrossRef](#)]
20. Ding, S.; Liu, L.; Zheng, W.X. Sliding Mode Direct Yaw-Moment Control Design for In-Wheel Electric Vehicles. *IEEE Trans. Ind. Electron.* **2017**, *64*, 6752–6762. [[CrossRef](#)]
21. Zhang, L.; Ding, H.; Shi, J.; Huang, Y.; Chen, H.; Guo, K.; Li, Q. An Adaptive Backstepping Sliding Mode Controller to Improve Vehicle Maneuverability and Stability via Torque Vectoring Control. *IEEE Trans. Veh. Technol.* **2020**, *69*, 2598–2612. [[CrossRef](#)]
22. Wang, Q.; Zhao, Y.; Deng, Y.; Xu, H.; Deng, H.; Lin, F. Optimal Coordinated Control of ARS and DYC for Four-Wheel Steer and In-Wheel Motor Driven Electric Vehicle With Unknown Tire Model. *IEEE Trans. Veh. Technol.* **2020**, *69*, 10809–10819. [[CrossRef](#)]
23. Rezaeian, A.; Zarringhalam, R.; Fallah, S.; Melek, W.; Khajepour, A.; Chen, S.-K.; Moshchuck, N.; Litkouhi, B. Novel Tire Force Estimation Strategy for Real-Time Implementation on Vehicle Applications. *IEEE Trans. Veh. Technol.* **2015**, *64*, 2231–2241. [[CrossRef](#)]
24. Cho, W.; Yoon, J.; Yim, S.; Koo, B.; Yi, K. Estimation of Tire Forces for Application to Vehicle Stability Control. *IEEE Trans. Veh. Technol.* **2010**, *59*, 638–649.
25. Doumiati, M.; Victorino, A.C.; Charara, A.; Lechner, D. Onboard Real-Time Estimation of Vehicle Lateral Tire/Road Forces and Sideslip Angle. *IEEE/ASME Trans. Mechatron.* **2011**, *16*, 601–614. [[CrossRef](#)]
26. Hamann, H.; Hedrick, J.K.; Rhode, S.; Gauterin, F. Tire force estimation for a passenger vehicle with the Unscented Kalman Filter. In Proceedings of the 2014 IEEE Intelligent Vehicles Symposium Proceedings, Dearborn, MI, USA, 8–11 June 2014; pp. 814–819.